Degradation study of a reversible solid oxide cell (rSOC) short stack using distribution of relaxation times (DRT) analysis

Sampathkumar, Suhas Niggehalli; Aubin, Philippe ; Couturier, Karine; Sun, Xiufu; Sudireddy, Bhaskar Reddy; Diethelm, Stefan; Pérez-Fortes, Mar; van Herle, Jan

DOI
10.1016/j.ijhydene.2022.01.104

Publication date
2022

Document Version
Final published version

Published in
International Journal of Hydrogen Energy

Citation (APA)
Sampathkumar, S. N., Aubin, P., Couturier, K., Sun, X., Sudireddy, B. R., Diethelm, S., Pérez-Fortes, M., & van Herle, J. (2022). Degradation study of a reversible solid oxide cell (rSOC) short stack using distribution of relaxation times (DRT) analysis. *International Journal of Hydrogen Energy*, *47*(18), 10175-10193. https://doi.org/10.1016/j.ijhydene.2022.01.104

Available online at www.sciencedirect.com

ScienceDirect

journal homepage: www.elsevier.com/locate/he

Degradation study of a reversible solid oxide cell (rSOC) short stack using distribution of relaxation times (DRT) analysis

Suhas Nuggehalli Sampathkumar [a,c,*], *Philippe Aubin* [a], *Karine Couturier* [b], *Xiufu Sun* [c], *Bhaskar Reddy Sudireddy* [c], *Stefan Diethelm* [a], *Mar Pérez-Fortes* [a], *Jan Van herle* [a]

[a] Group of Energy Materials, Swiss Federal Institute of Technology, Lausanne (EPFL), Sion 1951, Switzerland
[b] Univ. Grenoble Alpes – CEA/LITEN, 38054 Grenoble, France
[c] Department of Energy Conversion and Storage, Technical University of Denmark, 2800 Kgs. Lyngby, Denmark

HIGHLIGHTS

- Degradation analysis of state-of-the-art reversible solid oxide cell.
- Application of EIS/DRT to isolate loss mechanisms responsible for degradation.
- Degradation rate comparison for rSOC cycles and post-cycling steady-state SOEC mode.

GRAPHICAL ABSTRACT

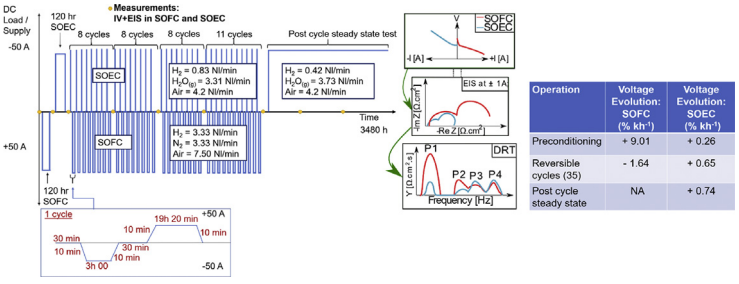

Operation	Voltage Evolution: SOFC (% kh^{-1})	Voltage Evolution: SOEC (% kh^{-1})
Preconditioning	+ 9.01	+ 0.26
Reversible cycles (35)	- 1.64	+ 0.65
Post cycle steady state	NA	+ 0.74

ARTICLE INFO

Article history:
Received 27 October 2021
Received in revised form
11 January 2022
Accepted 13 January 2022
Available online 8 February 2022

Keywords:
Reversible solid oxide cell
rSOC
Distribution of relaxation times
DRT
rSOC degradation

ABSTRACT

Reversible solid oxide cells (rSOC) can convert excess electricity to valuable fuels in electrolysis cell mode (SOEC) and reverse the reaction in fuel cell mode (SOFC). In this work, a five – cell rSOC short stack, integrating fuel electrode (Ni-YSZ) supported solid oxide cells (Ni-YSZ || YSZ | CGO || LSC-CGO) with an active area of 100 cm^2, is tested for cyclic durability. The fuel electrode gases of H_2/N_2:50/50 and H_2/H_2O:20/80 in SOFC and SOEC mode, respectively, are used during the 35 reversible operations. The voltage degradation of the rSOC is 1.64% kh^{-1} and 0.65% kh^{-1} in SOFC and SOEC mode, respectively, with fuel and steam utilisation of 52%. The post-cycle steady-state SOEC degradation of 0.74% kh^{-1} suggests improved lifetime during rSOC conditions. The distribution of relaxation times (DRT) analysis suggests charge transfer through the fuel electrode is responsible for the observed degradation.

* *Corresponding author*. Group of Energy Materials, Swiss Federal Institute of Technology, Lausanne (EPFL), Sion 1951, Switzerland
E-mail address: suhas.nuggehallisampathkumar@epfl.ch (S. Nuggehalli Sampathkumar).

https://doi.org/10.1016/j.ijhydene.2022.01.104

Abbreviations

PV	Photovoltaics
rSOC	Reversible solid oxide cell
SOFC	Solid oxide fuel cell
SOEC	Solid oxide electrolysis cell
SEM	Scanning Electron Microscopy
YSZ	Yttria-Stabilized Zirconia
3YSZ	3 mol% Yttria Stabilized Zirconia
LSM	Lanthanum Strontium Manganate air electrode or contact element: $(La_xSr_{1-x})MnO_{3-\delta}$
LSC	Lanthanum Strontium Cobalt current collector: $(La_{0.6}Sr_{0.4}CoO_{3-\delta})$
MIEC	Mixed ionic - electronic conductor
SoA	State of the art
ASR	Area specific resistance
EIS	Electrochemical impedance spectroscopy
DRT	Distribution of relaxation times
RU	Repeatable unit
OCV	Open Circuit Voltage
8YSZ	8 mol% Yttria Stabilized Zirconia electrolyte
CGO	Gadolinium Doped Ceria (CGO) barrier layer
LSCF	Lanthanum Strontium Cobalt Ferrite air electrode: $(La_xSr_{1-x})Co_yFe_{1-y}O_{3-\delta}$
LSC-CGO	LSC infiltrated with CGO air electrode: $(La_{0.6}Sr_{0.4}CoO_{3-\delta}$-$Ce_{0.9}Gd_{0.1}O_{2-\delta})$
IT-rSOC	Intermediate temperature – reversible solid oxide cell
SC	Single Cell
BC	Button Cell
SS	Short Stack
EIFER	European Institute for Energy Research

List of Symbols

R_{ohm}	Ohmic resistance
R_{pol}	Polarisation resistance
λ	Air excess ratio
$n_{O_2-stoichiometric}$	The stoichiometric number of moles of oxygen needed for complete conversion of hydrogen
$n_{O_2-supplied}$	The supplied number of moles of oxygen as a fraction of air flowrate
$d_{abs}(x)$	Absolute voltage degradation rate for the RU; $x = 1$ to 5 is the RU number
$d_{rel}(x)$	Relative voltage degradation rate for the RU; $x = 1$ to 5 is the RU number
S1–S9	Electrochemical characterisation steps from 1 to 9
$d_{rSOC}(abs)$	Total absolute voltage degradation of the rSOC
$d_{rSOC}(ASR)$	Total absolute ASR degradation of the rSOC
$\overline{d}_{rSOC}(abs)$	Average absolute voltage degradation per RU of the rSOC
$\overline{d}_{rSOC}(rel)$	Average relative voltage degradation per RU of the rSOC
$\overline{d}_{rSOC}(ASR)$	Average absolute ASR degradation per RU of the rSOC

Introduction

The deployment of renewable energy systems has been increasing over the past few years. Photovoltaics (PV) and onshore wind energy sectors are forecasted to undergo enormous growth between 2019 and 2024 [1]. The intermittent energy production problem associated with PV and wind needs to be addressed to avoid surplus electricity curtailment. Energy production curtailment due to demand and supply mismatch leads to low capacity factors between 10 and 50% for photovoltaics and wind energy installations. The average capacity factor for wind power plants is around 24.7%, and that of photovoltaics power plants is 18% which is lower compared to coal and nuclear electric power [1–5]. Reversible solid oxide cell (rSOC) systems are a promising solution for this problem. The rSOC systems operate in the solid oxide fuel cell (SOFC) mode generating electricity when the supply from renewable sources is limited. The system can also be utilised in solid oxide electrolysis cell (SOEC) mode during excess renewable electricity generation, producing useful precursors for fuel syntheses, such as hydrogen and other fuels as methane, methanol, ammonia, and syngas. Among these, hydrogen has been forecasted to be a crucial energy vector to facilitate carbon neutrality [6]. The rSOC system is the energy conversion component of the power-to-X-to-power system, which can be used with a smart grid to balance the electricity demand-supply ratio [7,8]. Dynamic system model studies have proposed the use of rSOC system for self-sustaining islanded building, seawater desalinisation plants, hydrogen injection into the natural gas grid, and even implementation in paper mills has been recently suggested [9–12].

In SOFC mode, hydrogen is oxidised at the fuel electrode while the oxygen is reduced at air electrode, as shown in Equations (1) and (2). The reaction is facilitated at triple-phase boundaries, starting with the adsorption of the gases on the active sites. The overall redox reaction is converting hydrogen into steam, as shown in Equation (3).

$$H_2 \rightarrow 2H^+ + 2e^- \quad (1)$$

$$\frac{1}{2}O_2 + 2e^- \rightarrow O^{2-} \quad (2)$$

$$H_2 + \frac{1}{2}O_2 \rightarrow H_2O \quad (3)$$

The deionised water is electrochemically converted by applying a voltage difference between the fuel and the air electrodes in the SOEC mode. The fuel gas composition is composed of a mixture of hydrogen and steam to avoid oxidation of nickel in the fuel electrode [13]. The steam is reduced to hydrogen at the fuel electrode by supplying electricity, as shown in Equation (4). The resulting oxide ion is transferred through the electrolyte and onto the air electrode, where oxygen evolution occurs, as indicated in Equation (5). The reaction steps in the SOEC mode differ from that of the SOFC mode. However, the overall redox reaction is the reverse of that in the SOFC mode, as indicated in Equation (6).

$$H_2O + 2e^- \rightarrow H_2 + O^{2-} \quad (4)$$

$$O^{2-} \rightarrow \frac{1}{2}O_2 + 2e^- \quad (5)$$

$$H_2O \rightarrow H_2 + \frac{1}{2}O_2 \quad (6)$$

At the system level, the degradation while operating the rSOC stack depends on the mode of operation, the number of cyclic operations, fuel composition, operating temperature, fuel utilisation or steam conversion, current density, fuel distribution, local fuel starvation, leaks and uncontrolled failures [14–19]. Generally, lower steam conversion and fuel utilisation levels lead to higher durability of the rSOC repeatable unit (RU) at the cost of system efficiency without recirculation [20]. The first grid-integrated rSOC system in the world was demonstrated by Boeing using modules from Sunfire in 2015 [21,22]. Two modules of 25 kW_{DC} SOFC (80 kW_{DC} SOEC) were used for which the LHV efficiency varied between 60.5 and 72% in the SOEC mode and a maximum of 49% in SOFC mode, respectively. Recently, for performance mapping the reversible SOLIDpower large stack module (SOEC: 74 kW_{DC}) was operated between 710 and 745 °C and reached fuel utilisation level of 90% (SOFC: 10.5 kW_{DC}) and steam conversion of 80% with hydrogen production rate of 39–52 kg day^{-1} [23]. A rSOC power plant established with 100% fuel utilisation in SOFC mode upon recirculation and with the ability to reach 90% steam conversion in the SOEC mode had an overall plant efficiency of 51%. The process efficiencies of SOFC and SOEC modes were 67.1% and 76%, respectively [24].

For rSOC to be a better competitor with compressed air energy storage system, pumped hydro storage, and batteries, the system efficiency must be higher than 80% [25]. To improve rSOC systems performance such that the overall efficiency is improved by 30%, identifying the degradation mechanism is crucial. Long-term system control strategies have also been studied and operating parameters are proposed to predict failures, increase durability, and reduce degradation at the single cell and short stack levels [13,26–28]. These models infer the need for a better understanding of rSOC degradation mechanisms.

The degradation of rSOC cells is mostly due to mechanical failures, nickel agglomeration/migration on the fuel electrode, segregation in the air electrode, loss of contact and electrode poisoning [29]. Novel rSOC electrode materials have also been developed to increase performance at intermediate temperatures (550–650 °C). The air electrode overpotential is the most significant contributor to losses at these temperature ranges [30]. The intermediate operating temperatures are obtained by changing air electrode architecture, porosity, implementing proton-conducting electrolyte ($BaCeO_3$-based materials), identifying the rate-determining steps for the air electrode reactions, and developing new mixed ionic-electronic conducting (MIEC) materials [31–35]. However, to achieve the durability of the current state of the art rSOC, further research and development of the intermediate temperature reversible solid oxide cells (IT-rSOC) are necessary.

The current state of the art (SoA) anode supported rSOC consists of Ni/YSZ cermet as the fuel electrode, yttria stabilized zirconia-gadolinium doped ceria (YSZ-CGO) as the electrolyte-barrier layer and lanthanum strontium manganate (LSM) or lanthanum strontium cobalt ferrite (LSCF) air electrode. The terminologies of fuel and air electrodes are used as the definition of SOFC anode and cathode reverses with changing mode of operation to SOEC in a rSOC. The microstructural degradation occurring by operating the rSOC at the thermoneutral point in SOEC mode can be reversed by cycling in the SOFC mode, as demonstrated by Graves et al. [36]. In the SOEC mode, the primary cause of degradation is related to the air electrode-electrolyte interface under anodic polarisation conditions. Numerous studies have been performed to analyse and isolate the degradation mechanisms [14,37–40]. Electrochemical impedance spectroscopy (EIS) is a useful technique in identifying the changes in the ohmic and polarisation resistances. The evolution of the EIS spectra along the duration of the experiment renders information related to degradation. However, the information related to the loss mechanism is convoluted in the EIS spectra. The deconvolution of the EIS spectra using the distribution of relaxation time analysis (DRT) can be employed to identify intrinsic loss mechanisms. Using DRT to analyse the degradation mechanisms, a post-test analysis requirement may be bypassed, if not wholly replaced, to identify the microstructural degradation phenomena [41]. DRT has been applied to single-cell tests extensively in identifying solid oxide cell behaviour, improving material properties and tuning equivalent circuit models [42–47]. Only a few studies have utilised DRT in identifying the trends in the degradation of the rSOC stack [48–50].

In this work, we attempt to analyse the degradation trend of a five-cell rSOC short-stack operated at 700 °C for a total duration of 3480 h. The evolution of the area-specific resistance (ASR) is identified using current density - voltage characteristic curves. Further, ohmic and polarisation resistances are quantified using electrochemical impedance spectroscopy measurements during the experiment. The distribution of relaxation time (DRT) is implemented on the EIS measurements to identify intrinsic loss mechanisms trends.

Materials and methods

The rSOC repeatable unit

In this study, a stack design developed by CEA is used for testing in reversible SOFC/SOEC operation. It was initially dedicated to SOEC operation but recently upgraded for reversible SOFC/SOEC operation, emphasising the decrease of the pressure drops, especially on the airside [51]. It is planar with cross-flow fields. The 5-cell short stack comprises four thin interconnects made of 0.2 mm AISI441 ferritic stainless-steel sheets with in-plane interconnect dimensions of 205 × 205 mm^2 and two thick endplates. Voltage probes were spot-welded to each interconnect to measure the voltage of each cell. Thermocouples (K-type) were located in holes drilled in the thick endplates to evaluate the stack temperature gradient. Five fuel electrode supported cells from DTU with a 100 × 100 mm^2 active surface area are inserted between the interconnects. The cell consists of a

~10 μm thin Ni-8YSZ fuel electrode with a ~300 μm thick Ni-3YSZ support layer. The ~10 μm thin electrolyte is made of YSZ. In between the electrolyte and the air electrode, a ~6 μm thin CGO ($Ce_{0.9}Gd_{0.1}O_{2-\delta}$) diffusion barrier layer is deposited. Those four first layers are fabricated by tape-casting method, co-sintered at ca. 1300 °C and cut into 120 mm × 120 mm cells using laser cutting. Subsequently, a ~30 μm thick LSC-CGO ($La_{0.6}Sr_{0.4}CoO_{3-\delta}$-$Ce_{0.9}Gd_{0.1}O_{2-\delta}$) air electrode is screen-printed on the CGO barrier layer and sintered at ca. 950 °C. Finally, an additional ~30 μm thick screen-printed LSC ($La_{0.6}Sr_{0.4}CoO_{3-\delta}$) contact layer completes the cell after sintering in air at ca. 950 °C, as represented in Fig. 1(a). A sample single solid oxide cell was imaged using scanning electron microscopy (SEM) observation to verify the fabrication process, as shown in Fig. 1(b).

A nickel grid (100 meshes·cm^{-2}) and an LSM layer with the same size as the electrodes are added as contact elements between interconnects and cells, on the fuel and air sides, respectively. A commercial ceramic glass Schott G018-311 is used for sealing, with a mica foil that ensures the electrical insulation between two adjacent interconnects and the precise positioning of cells. Additional information on stack design and experimental results on performance, durability and gas conversion rates can be found in previously published works [51–55]. The 5-cell stack was assembled and pre-tested on a test bench at CEA to shape the sealant, assess good electrical contact and reduce fuel electrodes before shipment to EPFL. Quality control was also performed, recording some J-V curves and EIS diagrams used as reference performances. Moreover, a self-compression system composed of rods, tubes and springs was developed by EPFL with CEA collaboration to allow the compression force application from the cold part outside the furnace during testing at EPFL. This system was mounted on the stack for safe transportation to EPFL and maintained adequate support of electrical contacts during the test there.

Experimental setup

Fig. 2(a) and (b) shows a view of the 5-cell stack when assembled with the self-compression system and ready for shipment. Compressed air, Hydrogen (99.999%) and Nitrogen (99.999%) were used at EPFL and gas flows were controlled by Voegtlin mass flow controllers. A provision was made to supply liquid deionised water to the evaporator for steam generation purposes. A damper system was used to minimise steam pulsation at the exit of the pump. The rSOC was placed in a furnace maintained at 700 °C. Thermocouples (K- type) were installed at different positions to verify the temperature distribution during the operation of the rSOC as indicated in Fig. 2(c) and (e). The reactant flow exhaust was condensed to separate the generated steam from unused reactants. The unused reactants were combusted in a burner using hot air exhaust from the rSOC. The electrochemical analysis of the five repeatable-unit rSOC short-stack was performed at EPFL using the setup configuration, as shown in Fig. 2(c). The actual setup used is shown in Fig. 2(d). The repeatable units (RU) were placed so that RU5 was on the bottom plate, as shown in Fig. 2(e).

The rSOC was tested at 700 °C with 50% H_2 and 50% N_2 in the SOFC mode and 20% H_2 with 80% H_2O in SOEC mode. Constant current tests were done at ±0.5 A cm^{-2} in SOEC and SOFC modes, respectively. The flowrates of H_2 and N_2 used in the SOFC mode were 3.33 Nl min^{-1} each, while 0.83 Nl min^{-1} of H_2 and 3.31 Nl min^{-1} of steam were used in the SOEC mode. The air flowrate used was 7.50 Nl min^{-1} and 4.2 Nl min^{-1} in the SOFC and SOEC modes respectively. The air excess ratio (λ) is defined, as shown in Equation (7).

$$\lambda = \frac{n_{O_2-supplied}}{n_{O_2-stoichiometric}} \tag{7}$$

where, $n_{O_2-stoichiometric}$ is the number of moles of oxygen needed for complete conversion of supplied hydrogen in the SOFC mode at −0.5 A cm^{-2} and $n_{O_2-supplied}$ is the number of moles of oxygen supplied as a fraction of the air flowrate using the mass flow controller. A summary of the experimental conditions for both the SOFC and SOEC modes are listed in Table 1.

The rSOC was characterised using J-V and electrochemical impedance spectroscopy (EIS) measurements at various experiment stages. By performing the EIS measurements close to open circuit voltage (OCV), the required RU material properties and processes can be defined [56]. The quality of the EIS spectra was verified using Kramer Krönig's test. The spectra were further corrected for inductive and capacitive behaviour and smoothened. The corrected spectra were used to plot the distribution of relaxation time (DRT) analysis using Tikhonov regularisation [41,57,58]. The methodology used to calculate the DRT can be found in the published work of Caliandro et al. [43]. The summary of the adapted methodology can be found in Fig. 3.

Degradation calculation

By measuring the voltage evolution over time, the change in absolute and relative degradation rates for individual RU was calculated using Equations (8) and (9) respectively. The degradation rates of individual RU give performance information of the rSOC stack. The total degradation rate of the rSOC short stack was calculated by summing the degradation rates of the RU, as shown in Equation (10). The average voltage degradation per RU was calculated, as shown in Equation (11). The change in area-specific resistance (ASR) can be calculated based on the absolute and relative voltage change by incorporating the current density. This information is essential for determining the durability of the five cell rSOC short stack.

$$\frac{\Delta U_{RUx}}{\Delta t} = \left(\frac{U_{RUx}(t_2) - U_{RUx}(t_1)}{t_2 - t_1}\right) \times 1000 = d_{abs}(x) \tag{8}$$

$$\frac{\left(\frac{\Delta U_{RUx}}{U_{RUx}(t_1)}\right)}{\Delta t} = \left(\frac{\left(\frac{U_{RUx}(t_2) - U_{RUx}(t_1)}{U_{RUx}(t_1)}\right)}{t_2 - t_1}\right) \times 1000 = d_{rel}(x) \tag{9}$$

where $x = 1$ to 5, is the number of the repeatable units in the 5-cell rSOC short stack; ΔU_{RUx} is the change in voltage levels for a RU between times t_1 and t_2, in millivolt [mV]; Δt is the time duration between t_2 and t_1, in kilohour [kh]. $U_{RU}(t_1)$ and $U_{RU}(t_2)$ is the voltage levels of the RU at times t_1 and t_2 in millivolt [mV].

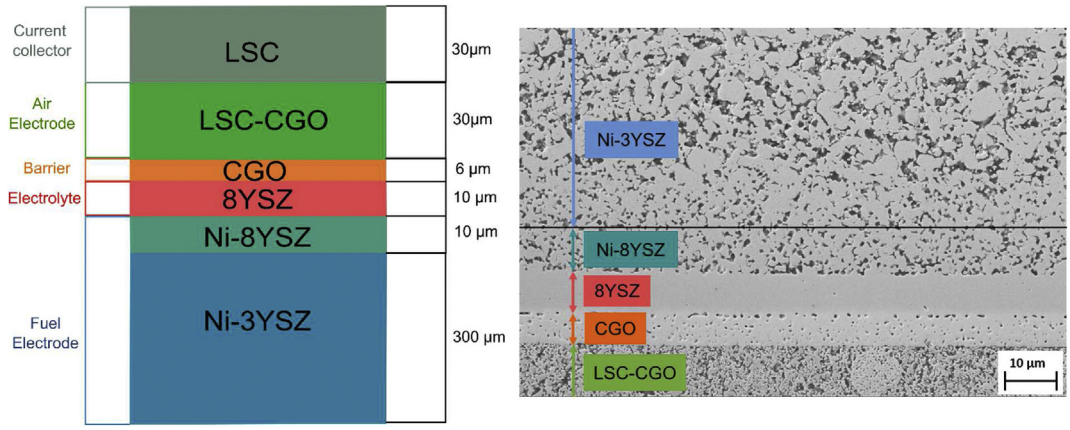

Fig. 1 – (a) The various layers present in one repeatable unit of the rSOC short stack, (b) the corresponding single cell scanning electron microscope (SEM).

The relative change in voltage is given by the $\frac{\Delta U_{RU}}{U_{RU}(t_1)}$, represented as a percentage change. Therefore, the units of absolute and relative degradations are represented as mV kh^{-1} and % kh^{-1}, respectively.

$$d_{rSOC}(abs) = \sum_{x=1}^{5} d_{abs}(x)$$
$$d_{rSOC}(ASR) = \frac{d_{rSOC}(abs)}{J} \quad (10)$$

where J is the current density of operation, ±0.5 A cm^{-2} based on the mode of operation.

$$\overline{d}_{rSOC}(abs) = \frac{d_{rSOC}(abs)}{total\ number\ of\ RU}$$
$$\overline{d}_{rSOC}(rel) = \frac{\sum_{x=1}^{5} d_{rel}(x)}{total\ number\ of\ RU} \quad (11)$$
$$\overline{d}_{rSOC}(ASR) = \frac{d_{rSOC}(ASR)}{total\ number\ of\ RU}$$

Results and discussion

Voltage evolution of the rSOC short stack

The rSOC short stack was initially subjected to steady-state testing starting with SOFC mode at +0.5 A cm^{-2} followed by SOEC mode at −0.5 A cm^{-2}, as shown in Fig. 4(i). The initial steady-state tests allow for preconditioning of all the RUs in the rSOC short stack [17]. Each mode was operated for 120 h. The J-V and EIS characterisation methods were performed before and after each steady-state mode (S1 to S3). After the initial steady-state modes, 35 rSOC cycles were performed between current densities of ±0.5 A cm^{-2}. Although some data points are missing due to data logging issues (M1 to M3), we firmly believe the tests have been conducted as planned.

Intermediate EIS measurements were performed after cycles 8, 16, 24 and 35 (S4 to S7). EIS measurements were also carried out in post-cycle steady state SOEC mode between S8 and S9. The summary of the measurement conditions is given in Table 2. The air preheater was changed after cycle 16 due to failure, and the new air preheater had reasonably performed the task. Due to this, there was air inlet temperature difference after cycle 16, compared to the initial cycles, as shown in Fig. 4(ii). This highlights the challenges associated with the balance of plants. The performance of the rSOC stabilized after one to two cycles of operation, after each EIS measurement. Therefore, degradation rates were calculated separately between cycles 3–16 and 18–35 for all the RU. The representation of the calculation window for the SOEC and SOFC modes, is shown in Fig. 4(a) and (b) and Fig. 4(c) and (d), respectively. The time period between which the degradation was calculated is represented between the dashed lines. The voltage degradation rate was calculated first between the beginning of cycles 3 and 16 (EC1:EC3 in SOEC mode and FC1:FC3 in SOFC mode). This operation was repeated between the ends of cycle 3 and 16 (EC2:EC4 and FC2:FC4). The two values were later averaged such that a single degradation rate in each mode between cycles 3–16 was found. The same method was adopted to calculate the voltage degradation rates between cycles 18–35.

As a whole, the rSOC short stack showed improvement or no degradation in cumulative performance in the initial steady-state conditions, as shown in Fig. 5(a) and (b), in both modes. The initial steady-state degradation rates revealed considerable performance improvement of 350 mV kh^{-1} in the SOFC mode for the whole stack. This performance improvement of all the RUs during preconditioning could be due to improved oxide (O^{2-}) ionic conductivity associated with YSZ in the electrolyte and the hydrogen electrode [59]. A positive degradation rate in the SOFC mode indicated performance improvement, while the same indicates degradation in the SOEC mode. As the rSOC short stack is in endothermal conditions in the SOEC mode, the temperature gradient across all the RUs influences the degradation rates. The temperature gradient is also impacted by the stack placement in the oven, with RU5 being close to the oven heat source compared to RU1. High voltage degradation was observed for RU1 and RU4 in the SOFC mode during the cyclic operation, while less than 0.5% kh^{-1} (4 mV kh^{-1}) were observed for the rest of the RUs. Performance decline in SOFC mode could be attributed to the

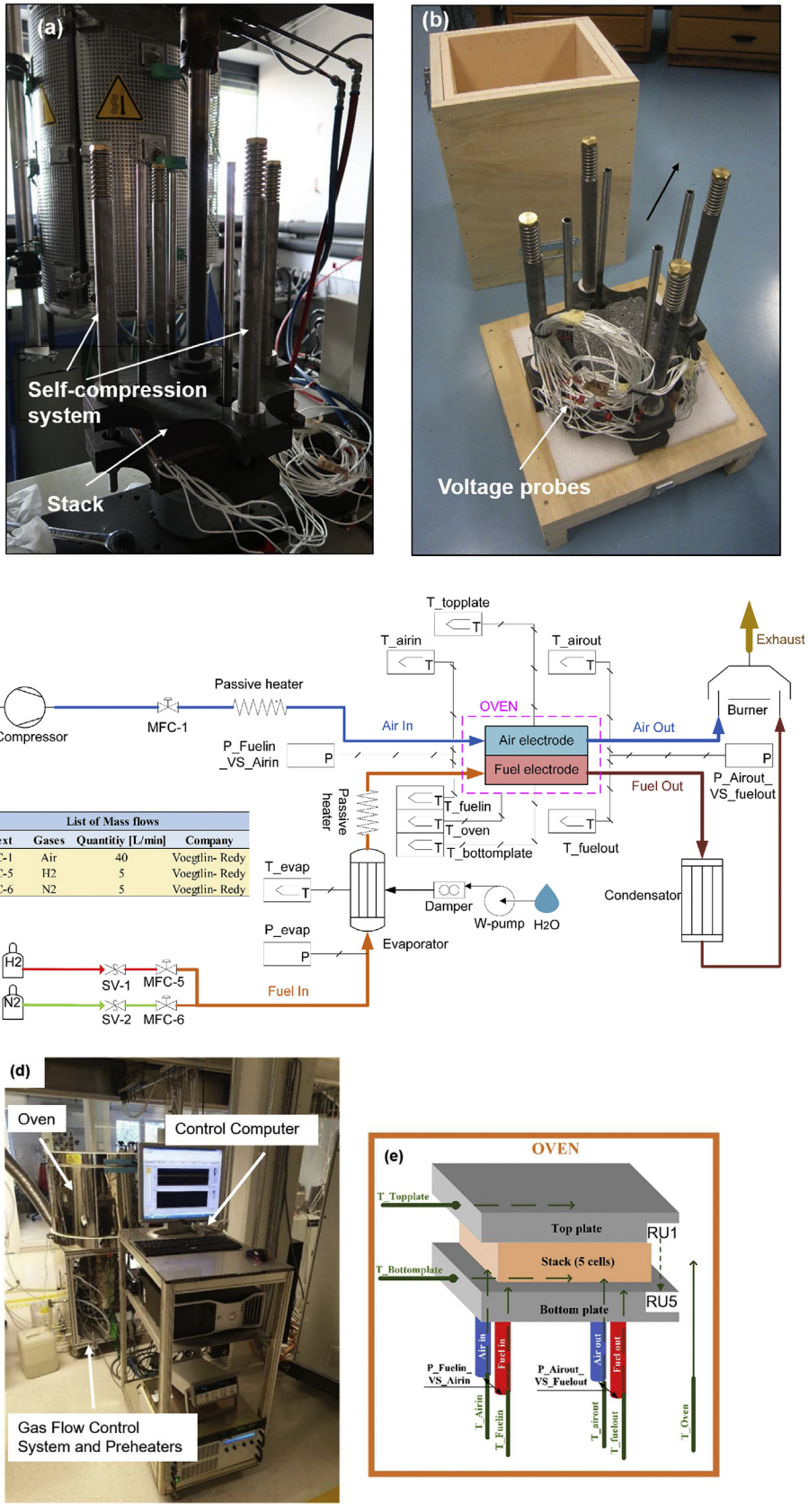

Fig. 2 – 5-cell stack with CEA design and DTU cells, (a) assembled to the self-compression system on a mechanical device and (b) ready to shipment to EPFL, (c) schematic representation of the rSOC short-stack testing facility at EPFL, (d) the experimental setup with oven, gas flow control system and the control computer at EPFL, (e) schematic representation of spatial placing of the RSOC short-stack and sensors.

Table 1 – Experimental Conditions for short stack rSOC in SOFC and SOEC modes.

Parameter	SOFC	SOEC
Current Bias rSOC operation	−50 A/-0.5 A cm^{-2}	+50 A/+0.5 A cm^{-2}
Current Bias EIS Measurements	−1 or −2 A/-0.01 or −0.02 A cm^{-2}	1 or 2 A/0.01 or 0.02 A cm^{-2}
Perturbation EIS Measurements	200 mA	1000 mA
Reactant Composition	H_2:N_2 = 50:50	H_2:H_2O = 20:80
Hydrogen Flowrate	3.33 Nl min^{-1}	0.83 Nl min^{-1}
Nitrogen Flowrate	3.33 Nl min^{-1}	0 Nl min^{-1}
Steam Flowrate	–	3.31 Nl min^{-1}
Water Flowrate to Evaporator	–	2.67 Nml min^{-1}
Air Flowrate	7.50 Nl min^{-1}	4.2 Nl min^{-1}
Air excess ratio (λ)	1	–
Experimental duration per cycle	19 h 20 min	3 h
Number of rSOC cycles	35	

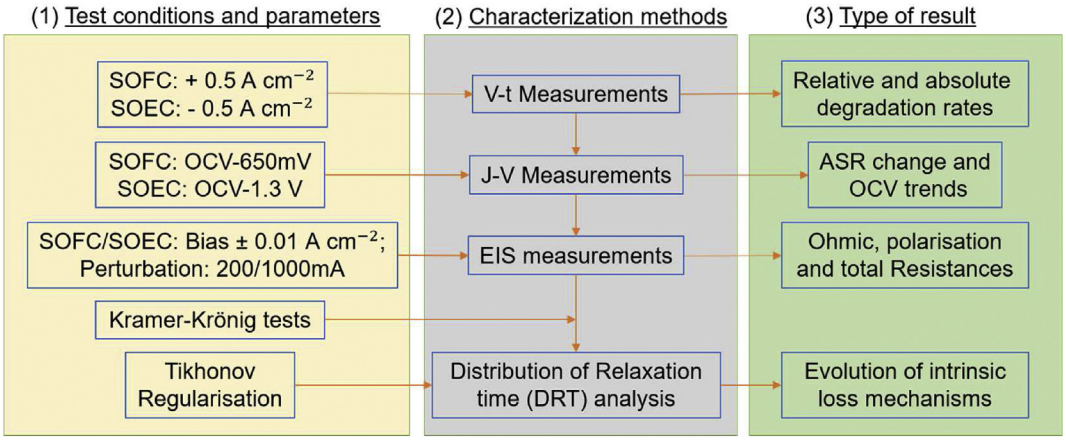

Fig. 3 – Workflow for rSOC characterisation and analysis.

damage caused in SOEC mode. The rSOC short stack cumulative degradation was about 45–70 mV kh^{-1} in SOFC mode and 27–65 mV kh^{-1} in SOEC mode for cycles 3–16 and 18–35. The average voltage degradation rate per RU of the rSOC short stack between cycles 3–35 was 1.64% kh^{-1} (11.44 mV kh^{-1}) in the SOFC mode and 0.65% kh^{-1} (9.11 mV kh^{-1}) in the SOEC mode. During the reversible operation, the overall ASR change was 114.41 mΩ cm^2 kh^{-1} and 91.06 mΩ cm^2 kh^{-1}, in SOFC and SOEC modes, respectively. These values are summarised in Table 3.

The rSOC was subjected to steady-state SOEC mode for 1506 h after the cyclic operation. The J-V and EIS measurements were taken at 2090 h (S8) and 2831 h (S9). The average voltage degradation rate of the rSOC during the post-cycle steady-state SOEC test was 0.74% kh^{-1} (6.60 mV kh^{-1}), which corresponded to a change in ASR level of 13.2 mΩ cm^2 kh^{-1}.

A comparison of the performance of the rSOC with the data from literature has shown variation in the quantities reported for similar SOFC material composition and operating conditions, as indicated in Table 4. From this work, the rSOC operation has shown degradation in SOEC mode to be about 0.65% kh^{-1}, which is among the lowest to the best of the authors' knowledge.

Area specific resistance, electrochemical impedance spectroscopy and distribution of relaxation time analysis

The characteristic J-V polarisation curve of the rSOC short stack, recorded sequentially, shows similar OCV and performance for all the RUs suggesting gas-tight seal and good integrity of each RU, as shown in Fig. 6. The OCV was around 1.25 V for the SOFC mode and 0.92 V for the SOEC mode. The difference in the OCV between the two modes is due to the usage of different compositions: dry gas (H_2:N_2 = 50:50) in SOFC mode and high quantity of steam (H_2O:H_2 = 80:20) in SOEC mode.

The area-specific resistances calculated at 0.4 A cm^{-2} increased progressively during the preconditioning and the cyclic operations, as shown in Figure A1 of the Appendix. The OCV and ASR levels decrease from RU1 to 5, suggesting the thermal gradient effects across the stack. During the post-cycle steady-state SOEC mode test, the gas composition was changed to H_2O:H_2 = 90:10. The decrease in H_2 volume fraction by 10% increase in the steam volume fraction resulted in a drop in OCV during the post-cycle steady-state SOEC mode of operation [63]. As RU3 is the geometric centre of the rSOC short-stack and had a good performance in both modes, it will

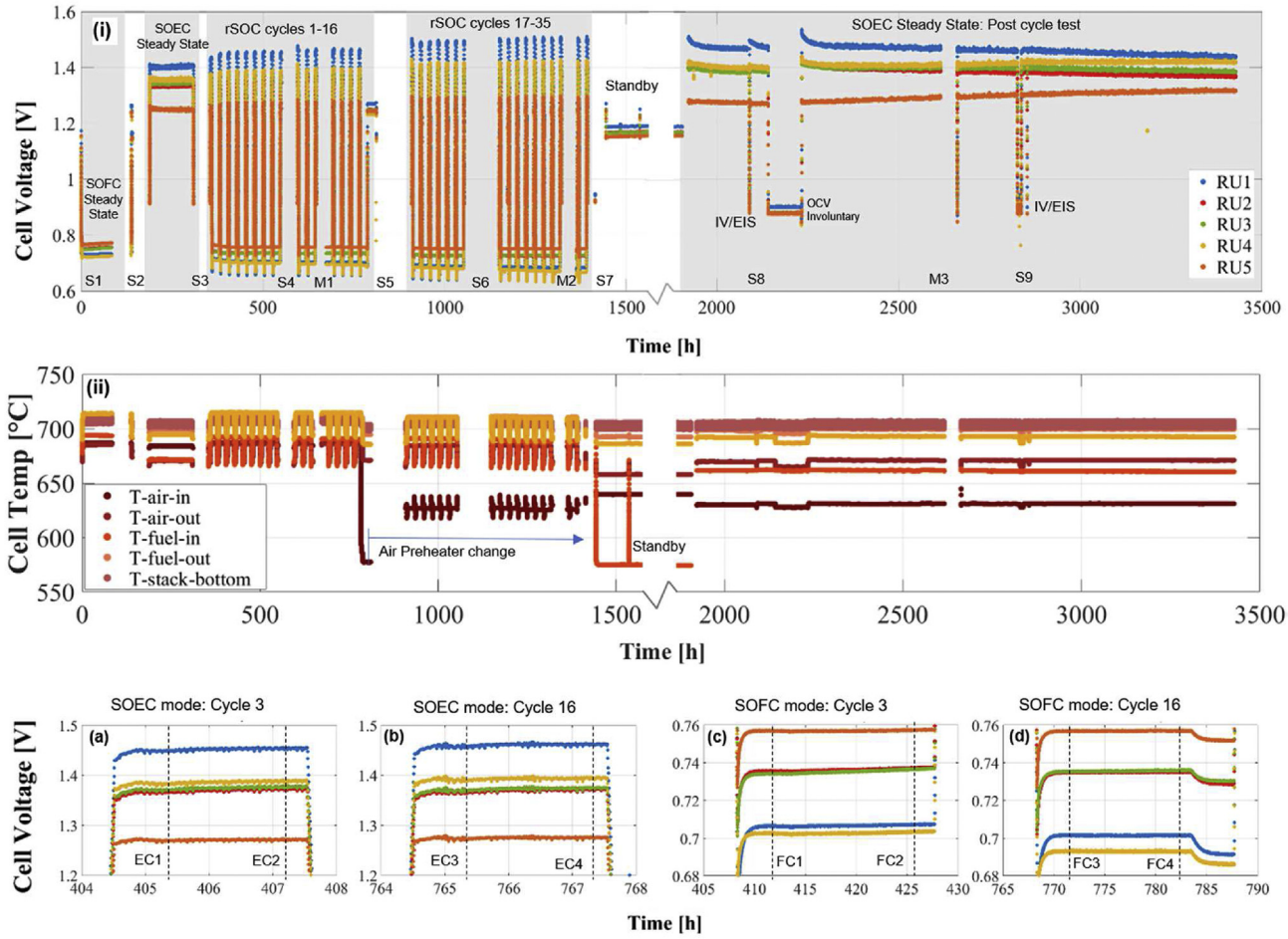

Fig. 4 – i) The voltage versus time characteristics of the 5 cell rSOC Short Stack showing the steady state and cyclic operations along the experimental duration of 3480 h. The J-V and EIS characterizations were performed at various steps (S1 to S9). ii) The temperature versus time characteristics of the 5-cell rSOC short stack during the experiment. Graphs (a) and (b) represent the V-t characteristics of the rSOC short stack in SOEC mode zoomed on cycles 3 (EC1-EC2) and 16 (EC3-EC4). Graphs (c) and (d) represent the V-t characteristics of the rSOC short stack in SOFC mode zoomed on cycles 3 (FC1-FC2) and 16 (FC3-FC4). Vertical lines suggest the window of degradation calculation for a cycle.

Table 2 – The electrochemical impedance spectroscopy (EIS) measurement conditions across steps S1 to S9.

Steps	Time (h)	SOFC mode		SOEC mode	
		EIS Bias (A cm^{-2})	EIS Perturbation (mA)	EIS Bias (A cm^{-2})	EIS Perturbation (mA)
S1	0	(S1 to S5) 0.01	(S1 to S7) 200	(S1 to S4) 0.01	(S1 to S9) 1000
S2	120				
S3	350				
S4	570				
S5	800			(S5 to S9) 0.02	
S6	1150	0.02			
S7	1400	0.01			
S8	2200	–	–		
S9	2900	–	–		

be investigated further while information about the other RU is given in the Appendix.

The quantification of the change in ASR is possible through EIS. The EIS spectrum is a Nyquist plot through which the ohmic, polarisation and total resistances of the RUs can also be quantified. The EIS spectrum for both modes was affected by high-frequency inductance for all the RUs [64]. The noise due to steam generation in SOEC mode was predominant at frequencies lower than 10 Hz. The current and voltage leads were twisted to minimise the cable inductive effect. In response, capacitive behaviour is observed during EIS measurement at high frequency, as shown in Appendix Figure A2.

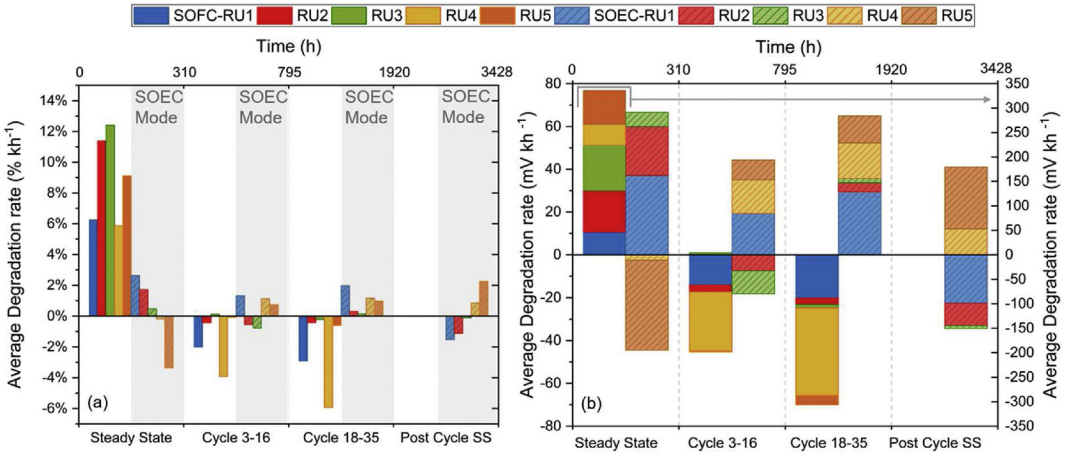

Fig. 5 – The evolution of voltage degradation along the duration of the experiment in both modes represented in (a) voltage change percentage per kilohour (% kh^{-1}) and (b) voltage change per kilohour (mV kh^{-1}).

Table 3 – Average Voltage and ASR degradation rates between cycles 1–35 in SOFC and SOEC modes.

Mode	Cycles	3 to 35			per cycle		
	Units	(Avg. Relative) % kh^{-1}	(Absolute) mV kh^{-1}	(ASR) mΩ cm^2 kh^{-1}	(Avg. Relative) % kh^{-1}	(Absolute) mV kh^{-1}	(ASR) mΩ cm^2 kh^{-1}
SOFC	Avg. Degradation per RU ($\bar{d}_{rSOC}$)	−1.64 (−0.81[a])	−11.44 (−5.77[a])	22.88 (11.54[a])	−0.10 (−0.03[a])	−0.72 (−0.36[a])	1.43 (1.37[a])
	rSOC Degradation (d_{rSOC})		−57.20 (−23.09[a])	114.41 (46.17[a])		−3.58 (−1.44[a])	7.15 (0.72[a])
SOEC	Avg. Degradation per RU ($\bar{d}_{rSOC}$)	0.65	9.11	18.21	0.04	0.57	1.14
	rSOC Degradation (d_{rSOC})		45.53	91.06		2.85	5.69

[a] Voltage degradation rates excluding RU4.

Table 4 – Degradation results found in literature for similar operating conditions.

Operation		Conditions				Degradation		Ref.
Type	Operating Mode	Materials [Fuel electrode || electrolyte || air electrode]	Temp. [°C]	Composition [$H_2/H_2O/N_2$] [%/%/%]	Current density [A/cm^2]/SC or FU [%]	mV kh^{-1}	% kh^{-1}	
Single cell (SC)	SOEC Steady-State	Ni-YSZ || YSZ || LSC-CGO	700	20/80/0	±0.5/52	–	7.7[b]	[17,60–62],[a]
	SOFC Steady-State			50/0/50		–	1.7[b]	
	SOEC reversible op.[c]			20/80/0		–	7	
	SOFC reversible op.[c]			50/0/50		–	3.8	
Button Cell (BC)	SOEC Steady-State	Ni-YSZ || YSZ || LSCF-GDC	750	10/90/0	- 0.75/48	60	41	
SC					−0.5/n.a.	21	–	
Short stack (SS) (EPFL)					−0.7/41	17	–	
SS (EIFER)					−0.5/n.a.	–	<1	
SS	SOFC Steady-State	Ni -YSZ || YSZ || LSM-YSZ	700	90-97/3–10/0	0.5/40	44	–	
SS	SOFC Steady-State	Ni-YSZ || YSZ || LCN-YSZ	750	100/0/0	0.37/10	–	1.7	

[a] There are more results available in these publications, however, only the most similar conditions are presented here.
[b] These results are measured over only 120 h.
[c] The cycles consisted of 3 h in FC mode and 20 h in EC mode per cycle.

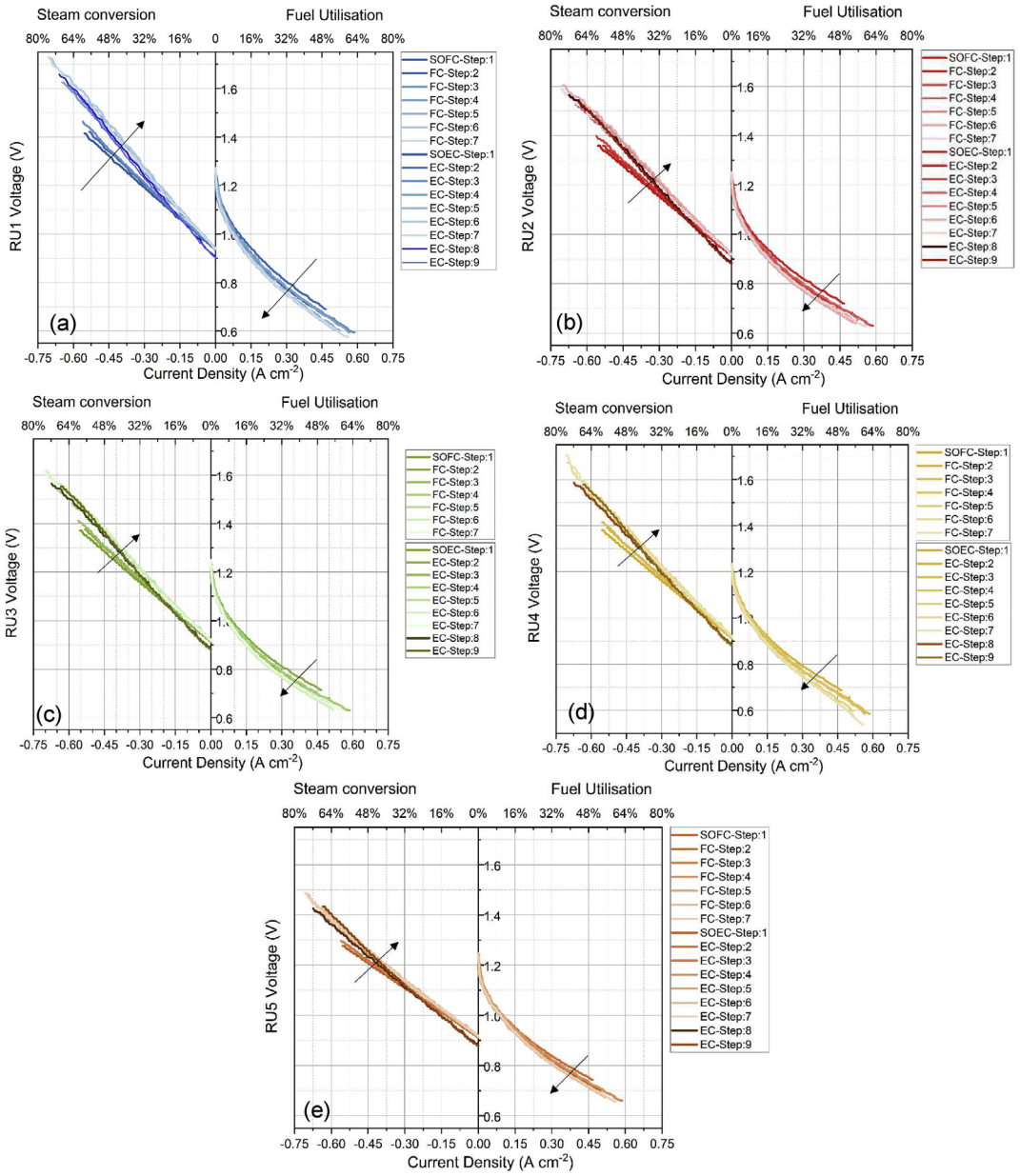

Fig. 6 – The polarisation curves for RU1-5 during the cycling operation (step 1 to 7) in both modes are shown in (a) to (d). The polarisation curves at the beginning and the end of the post-cycling steady-state SOEC mode are indicated at step 8–9. The corresponding steam conversion and fuel utilisation levels are also indicated on the top x axis.

The high-frequency capacitive effect was trimmed, and the spectra were *extended* based on the curvature of the high-frequency EIS arc. The low frequency noise due to steam generation was trimmed, smoothed, corrected for all the RUs, as shown in Figure A3 of the Appendix. The Kramer's Krönig residuals varied between ±3% in SOFC mode. The variation was ±2% for frequencies higher than 30 Hz and ±4% for a frequency range between 0.01 and 30 Hz in the SOEC mode.

The inductance and capacitance corrected Nyquist plots of the EIS measurements for both modes showed stable ohmic resistance after the initial preconditioning, while the polarisation resistance increased from S1 to S7, as shown in Fig. 7(a) and (b). The EIS measurements of S6 in SOFC mode were conducted with 2A bias to verify data quality improvement. The polarisation resistance (R_{pol}) in the SOFC mode appears to be larger by a factor of 10 than in the SOEC mode. This difference is primarily attributed to the low-frequency physical process resistances in the SOFC mode. The Bode plots clearly show the difference in the gas conversion resistances at a low frequency range below 10 Hz, as shown in Fig. 7(c) and (d). The presence of 80% steam in 20% H_2 significantly reduces the low-frequency impedance in the SOEC mode. Besides, degradation of RU3 in the intermediate frequency range of 10–100 Hz in SOFC mode, and at higher frequency range of 100 Hz to 10 kHz in SOEC mode is also observed. As expected, the Bode plots for all the RUs show similar trends in both modes, as indicated in

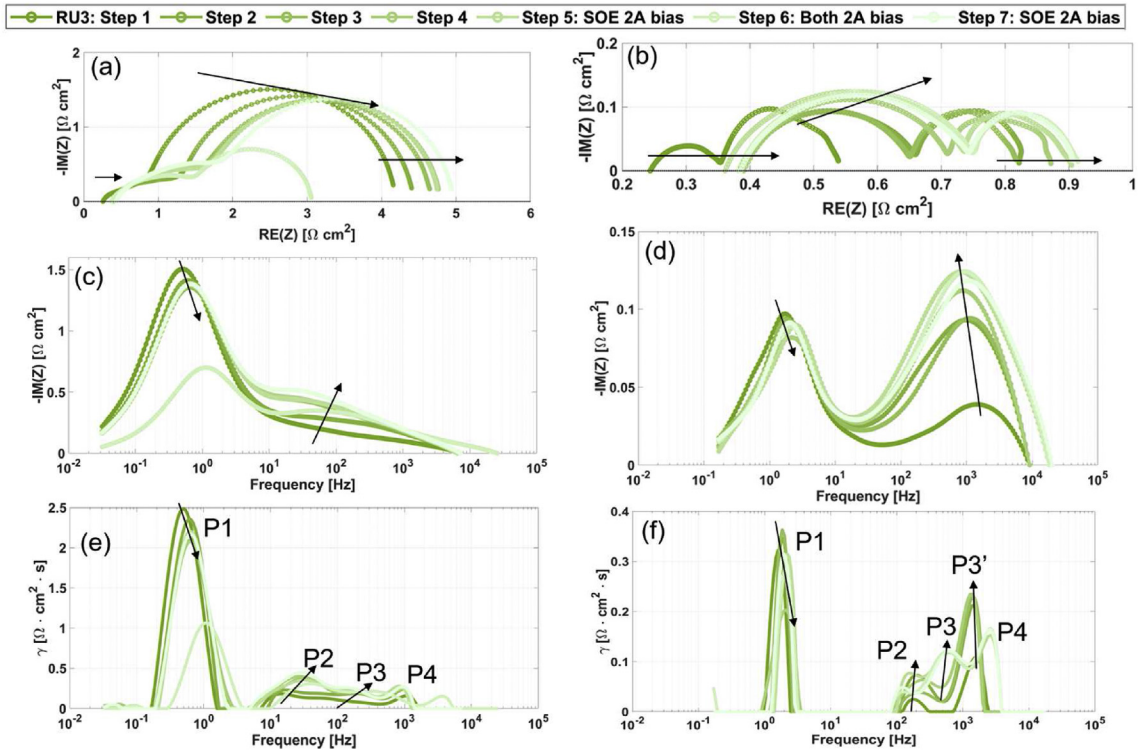

Fig. 7 – The performance of RU3 of the rSOC short stack in SOFC mode (a), (c) and (e) and SOEC mode (b), (d) and (f) from step 1 to 7. The inductance and capacitance corrected impedance spectra for the respective modes are shown in (a) and (b) as Nyquist plots, the variation of impedance as a function of frequency is represented by the Bode plots (c) and (d), and the corresponding distribution of relaxation times (DRT) is represented in (e) and (f).

Table 5 – DRT peak description and their respective range of frequencies, adapted from Refs. [43,65–67].

Peak no.	Peak range (Hz)	Peak Description
P1	10^{-1} - 10^{1}	Gas conversion resistance peak.
P2	10^{1}–10^{2}	Oxygen-surface exchange and oxide ion transport resistance in the air (LSC-CGO) electrode.
P3	10^{2}–10^{3}	Charge transfer resistance peak attributed to fuel (Ni-YSZ) electrode.
P4	> 10^{3}	Oxide ion transfer resistance peak attributed to air (LSC-CGO) and fuel (Ni-YSZ) electrode.

Figure A4 of the Appendix. The increase in resistance around 1 kHz corresponds to the charge transfer resistance at the H_2 electrode-electrolyte interface.

The *extended* EIS spectra were used to calculate the distribution of relaxation times (DRT) based on Tikhonov regularisation which helped in the deconvolution of various intrinsic processes. In both modes, the presence of four prominent peaks - P1 to P4 - was observed in Fig. 7(e) and (f), and the high frequency regime degrades. The four loss mechanisms identity was adapted from single-cell tests done in previous works [43,65,66] and listed in Table 5. The gas conversion resistance peak (P1) is distinctively observed in both modes near the frequency range of 0.1–10 Hz. Between the SOFC and the SOEC modes a considerable reduction in the gas conversion resistance (P1) is observed due to change in fuel composition. In the SOFC mode, the change in applied bias at S6 lowers the gas conversion peak P1 due to the evolution of gas composition from very dry to steam generation conditions and shifts the spectra towards higher frequencies. In the SOEC mode, from S1 to S4 the peaks of P3 and P4 are not distinguishable (P3′), suggesting nearby time constant values [67] of the charge transfer (P3) and oxide ion transfer processes (P4). The oxide ion transfer resistance peak (P4), associated with the air and fuel electrode, is seen at the end of the experiment. Upon increasing the bias from 0.01 to 0.02 A cm^{-2}, the charge transfer resistance (P3) and oxide ion transfer processes (P4) deconvolute from P3′. Previous studies have reported a similar change in charge transfer resistance (P3) based on operating current density [43,68].

The increase in P3 and P4 peaks resistance indicates degradation of the Ni-YSZ triple phase boundary, suggesting nickel agglomeration, loss of Ni–Ni connections or contamination. The degradation loss mechanisms trend for the rest of the RUs is similar, as indicated in Figure A5 of the Appendix.

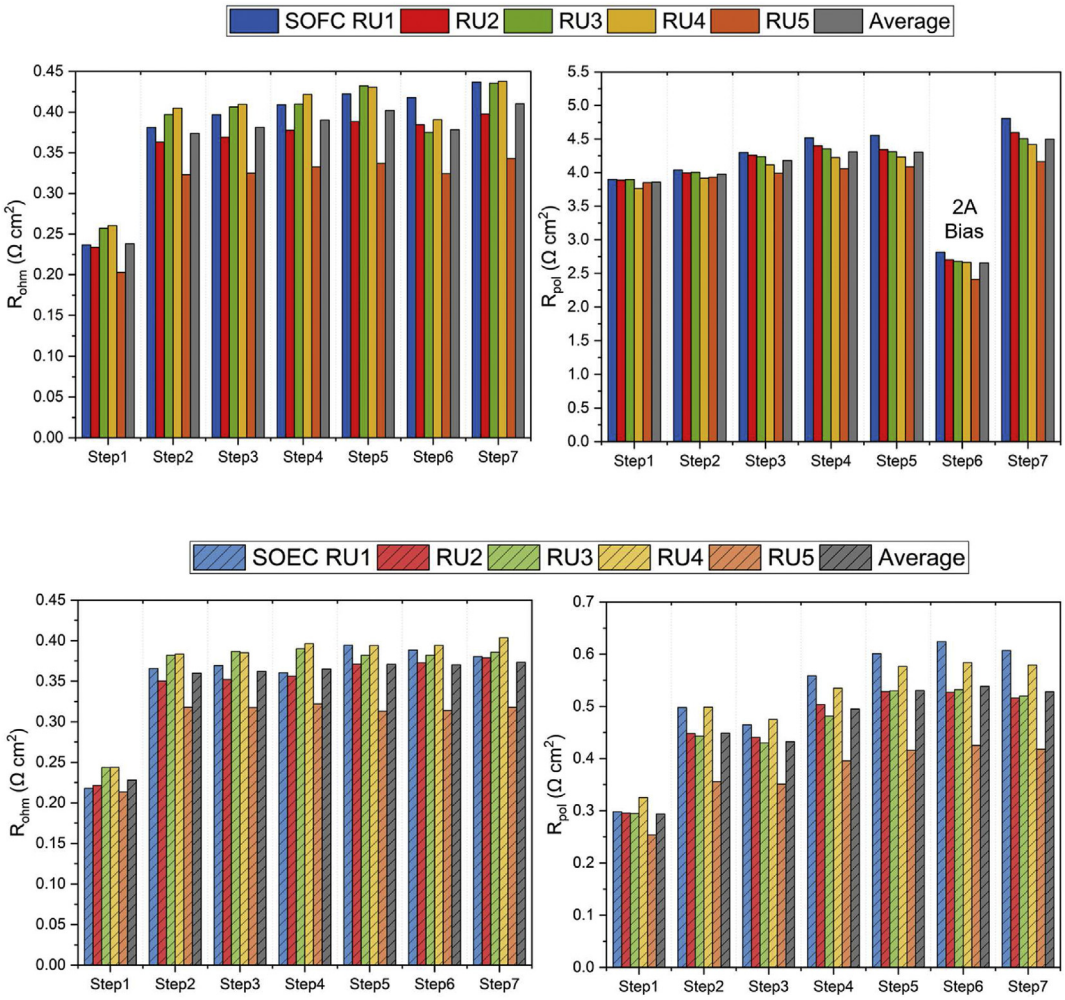

Fig. 8 – The (left) ohmic and (right) polarisation resistances of the rSOC short stack calculated from inductance and capacitance corrected Nyquist plots, in (top) SOFC mode and (bottom) SOEC mode.

The evolution of the ohmic and polarisation resistances determines the performance of the rSOC. After preconditioning, both R_{pol} and R_{ohm} increased for all the RUs in both modes, as shown in Fig. 8. The ohmic resistance remained consistent during the cyclic operation with minor fluctuations. The conditions might slightly vary between cells as individual measurements were performed sequentially. The polarisation resistance increased during the cyclic operation. The polarisation resistance changed following the increase in bias due to change in gas composition, heat generation or absorption based on the mode of operation. However, the change in bias did not affect the SOEC mode suggesting different reaction kinetics contributing to the polarisation resistance and less sensitivity towards gas conversion.

Post-cycling steady-state electrolysis

After the cyclic operation in the SOFC and SOEC mode, the rSOC was subjected to steady-state SOEC mode with a gas composition of H_2O:H_2 = 90:10 on the fuel electrode and an air flowrate for $\lambda < 1$. The change of gas composition helps in understanding the performance of the rSOC under lower hydrogen content. The ohmic resistances calculated from the EIS spectra have remained constant between S7 and S8 even after changing the gas composition, comparing Fig. 9 and Fig. 8.

However, the ohmic resistance of RU1 and RU3 increased considerably between S8 and S9, suggesting degradation due to loss of contact. Surprisingly, rSOC short stack performance improved between S8 and S9 with an average reduction in polarisation resistance of 9%. The Bode plots showed no change with the gas conversion peak (P1). It appears that the steady-state SOEC mode reduced the variation in the charge transfer resistance region across the RUs between S8 and S9. The Bode plots between the range of 100–30 000 Hz shrank closer amongst the RUs. Further, the DRT spectra analysis indicates that the charge transfer resistance (P3) reduced between S8 and S9. The peak P4 overlaps indistinguishably from RU1 to 5. As discussed earlier in Fig. 7, during reversible cyclic operation, the charge transfer resistance in fuel electrode (P3) and ionic transport in the air electrode (P2) showed increasing

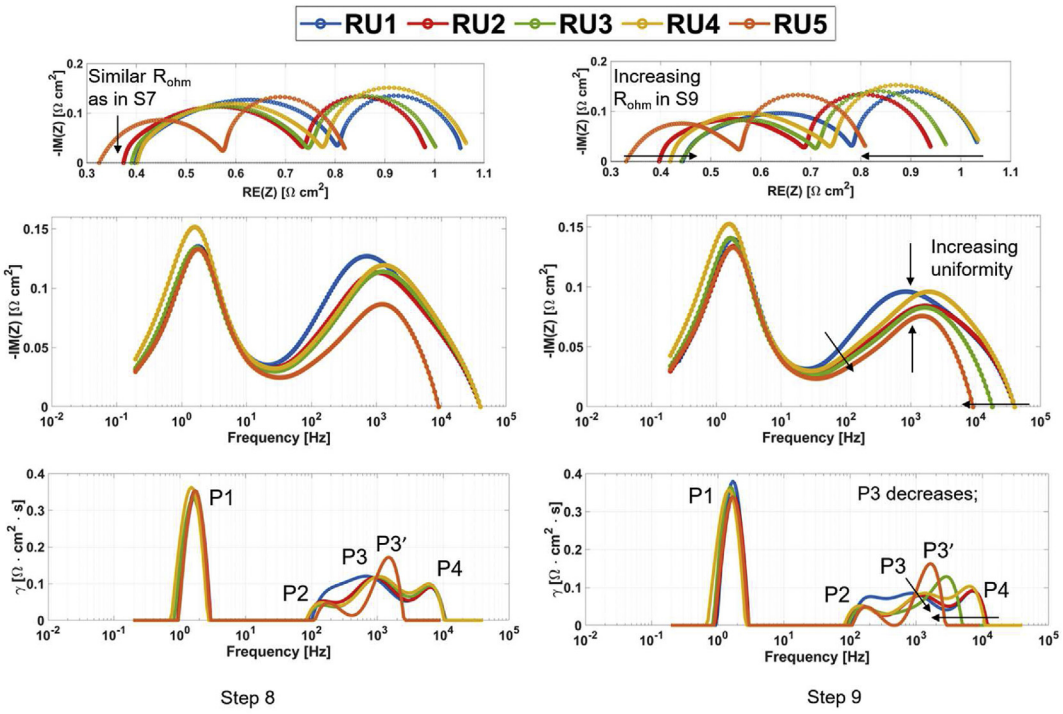

Fig. 9 – The performance of all the RUs in SOEC mode (left) at the beginning of the post-cycling test (S8) and (right) after 720 h into the post-cycling test (S9). (From top to bottom) The inductance and capacitance corrected Nyquist plots, the resulting Bode plots and the corresponding DRT plots are indicated with trends across the short stack.

trends. During the post cycling steady state SOEC mode, the decrease in P3 was higher while P2 was nearly constant. Overall, it was quite evident that the charge transfer through the fuel electrode (P3) is responsible for the observed degradation for all the RUs.

Conclusion

A five repeatable unit rSOC short stack was tested under cyclic conditions at 52% fuel utilisation (SOFC mode) or steam conversion (SOEC mode) at 700 °C and ±0.5 A cm^{-2}. The 35 operating cycles were performed with the fuel gas composition of H_2/N_2:50/50 in SOFC mode and H_2/H_2O:20/80 in SOEC mode. The current density-voltage measurements and electrochemical impedance spectroscopy (EIS) measurements were performed in both modes at regular intervals. The initial preconditioning operation revealed performance drop due to operation in SOEC mode. During the cyclic operation operating the rSOC in the SOFC mode reduced the SOEC mode degradation to less than 2% kh^{-1}. The EIS spectra deconvolution by Distribution of Relaxation Time (DRT) analysis suggested that the charge transfer in the fuel electrode (P3) and ionic transport in the air electrode (P2) is responsible for the observed degradation for all the RUs during cyclic operation. The post-cycling steady-state SOEC operation revealed changes only in charge transfer through the fuel electrode, suggesting P3 as the primary contributor for degradation of rSOCs.

Declaration of competing interest

The authors declare that they have no known competing financial interests or personal relationships that could have appeared to influence the work reported in this paper.

Acknowledgement

This project has received funding from the European Union's Horizon 2020 research and innovation programme under grant agreement No 731224.

Call identifier: H2020: LCE-2016-2017: LCE-33-2016.

The Swiss State Secretariat funds Swiss partners for Education, Research and Innovation SEFRI under contract 16.0178, 731224.

The authors would like to warmly acknowledge the expertise of Mr David Constantin in the development of the experimental setup at EPFL.

The authors would also like to sincerely acknowledge Ms Priscilla Caliandro and Mr Guillaume Jeanmonod for the development and optimisation of the distribution of relaxation time analysis code.

Appendix

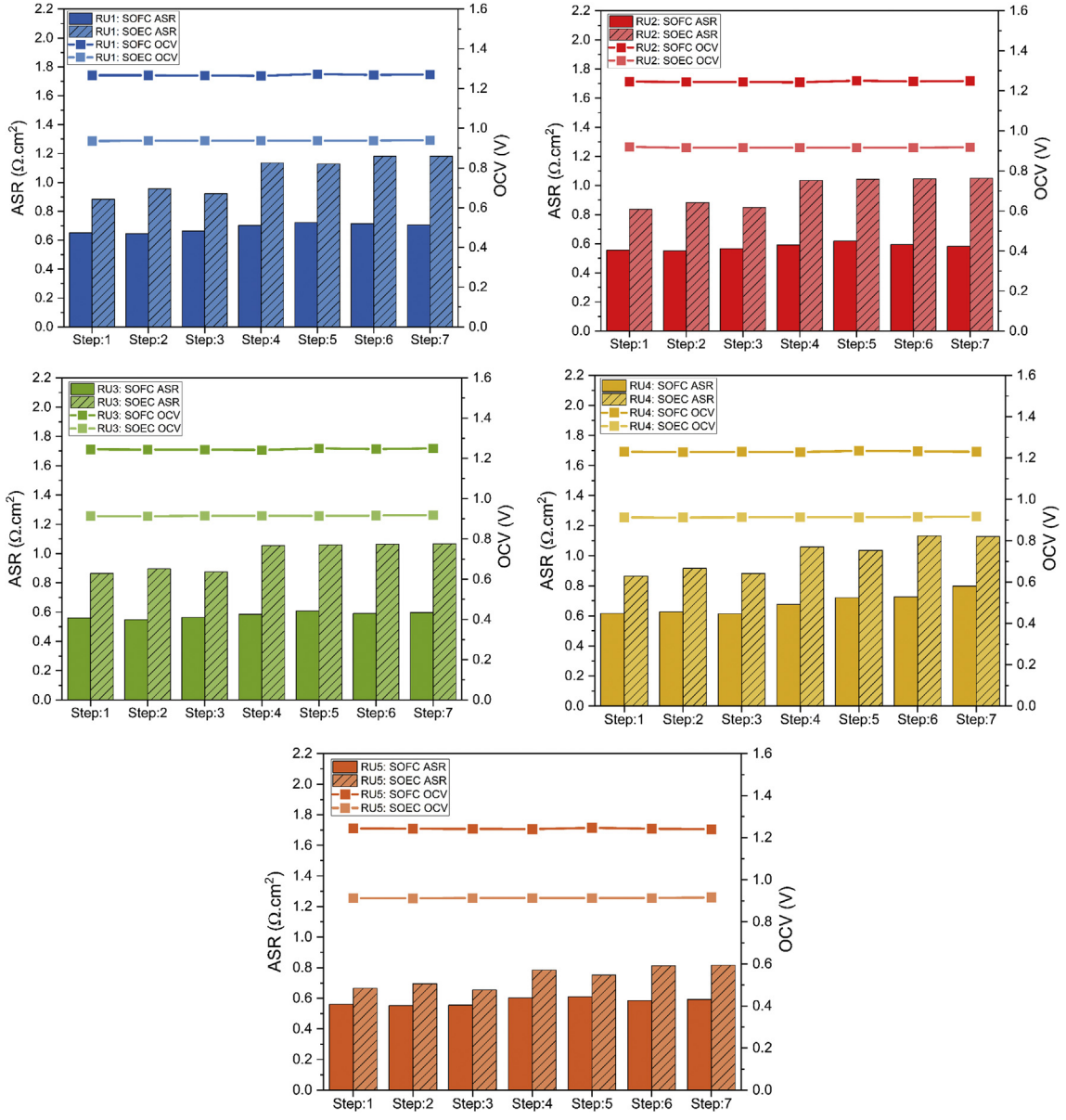

Figure A1 – The evolution of the area specific resistance and the stability of open circuit voltage values between steps 1 to 7. The ASR was calculated at ±0.4 A cm^{-2}. The ASR is measured in the linear part of the polarisation curve.

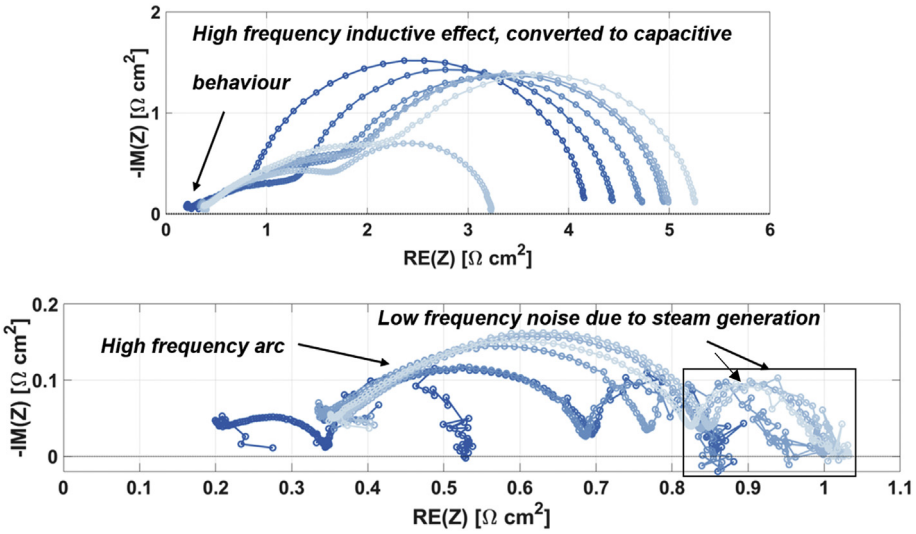

Figure A2 – The Nyquist plots of EIS spectra of RU1 from S1 to S7 in (top) SOFC mode affected by high frequency inductance and (bottom) in SOEC mode affected by low frequency noise due to steam generation.

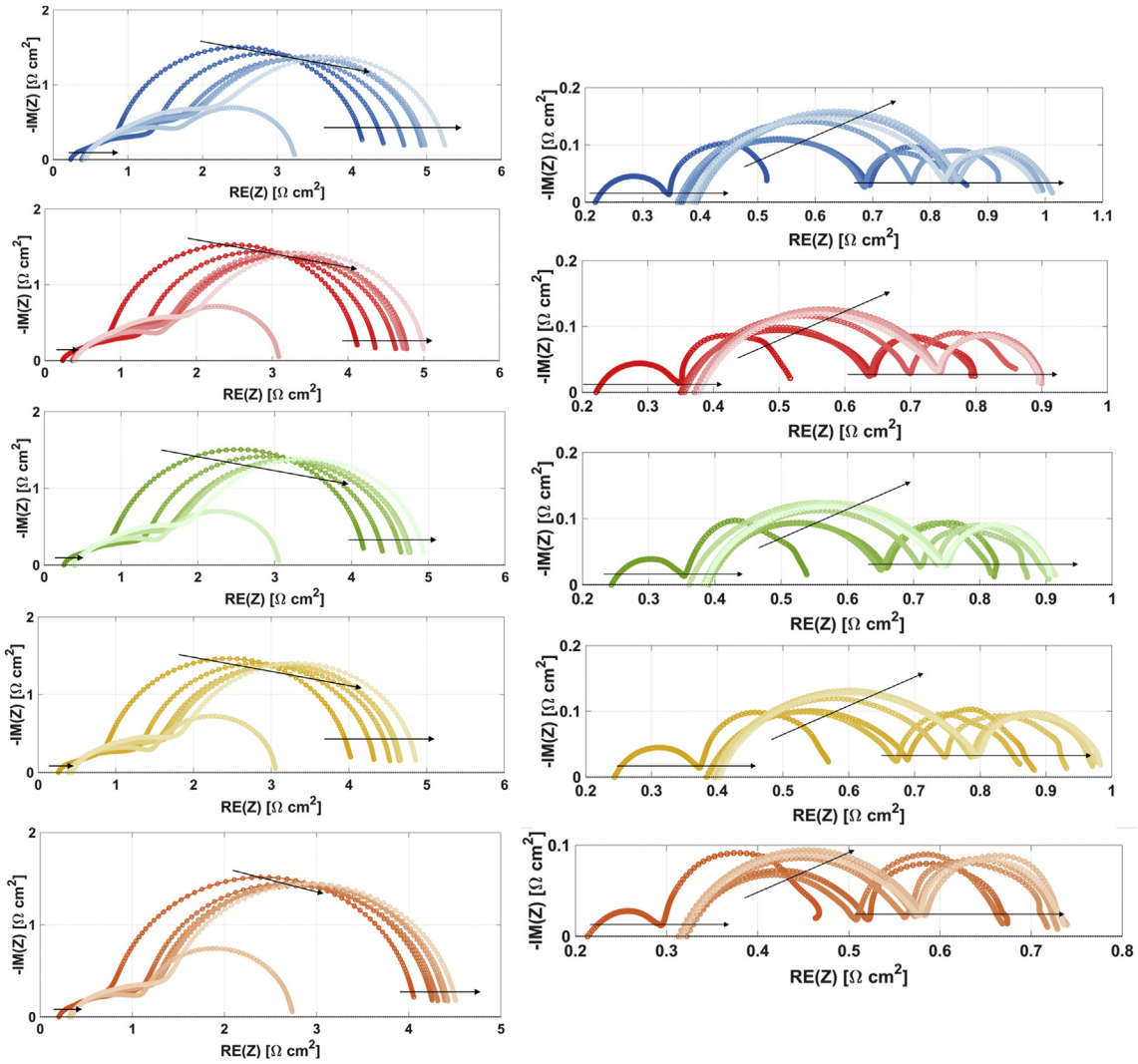

Figure A3 – The inductance, capacitive and low frequency noise corrected Nyquist plots of the EIS measurements for RU1 to 5 (top to bottom), in SOFC mode (left) and SOEC mode (right).

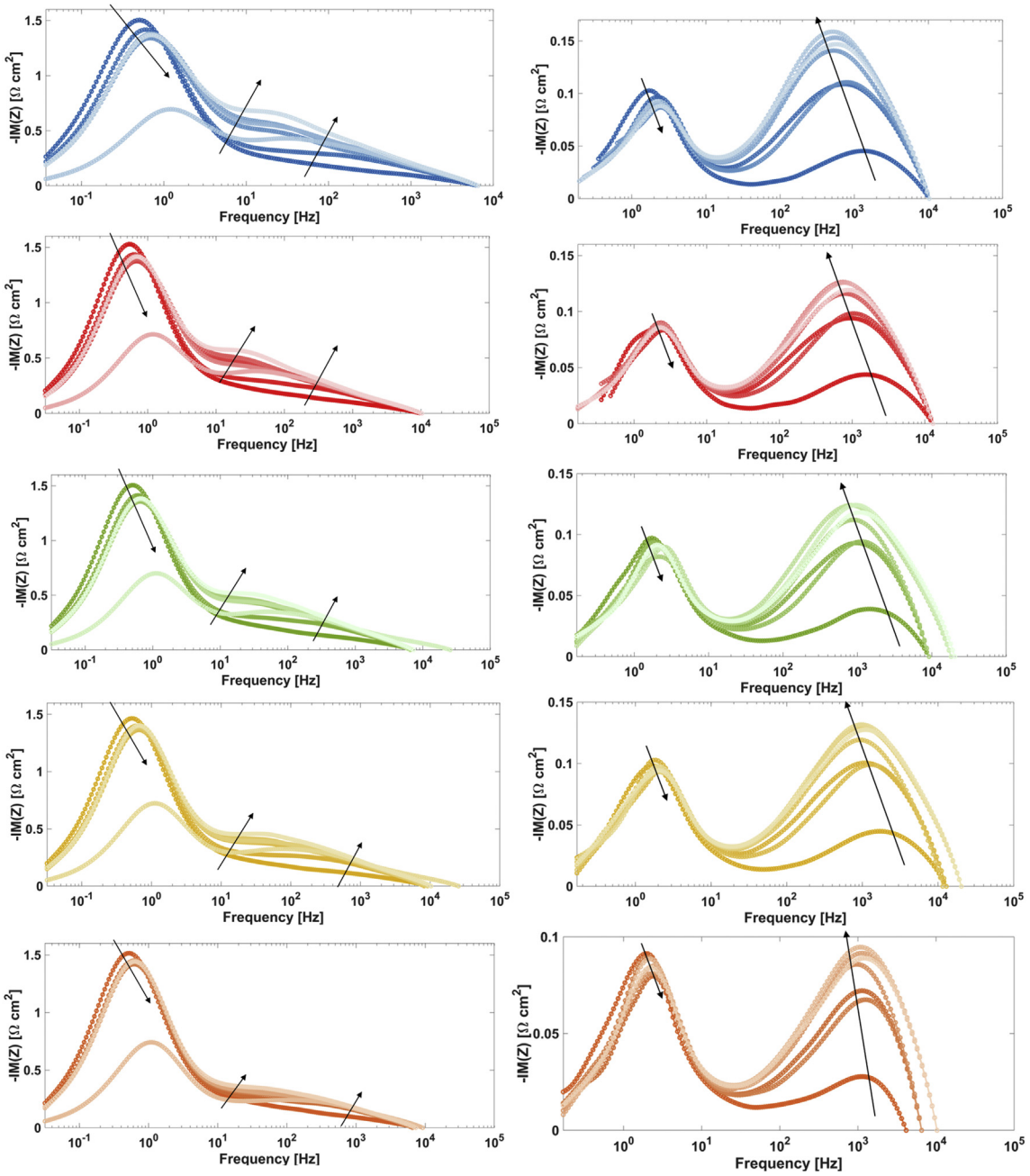

Figure A4 – The inductance and capacitance corrected Bode plot for RU1 to RU5 (top to bottom) in SOFC mode (left) and SOEC mode (right) from S1 to S7.

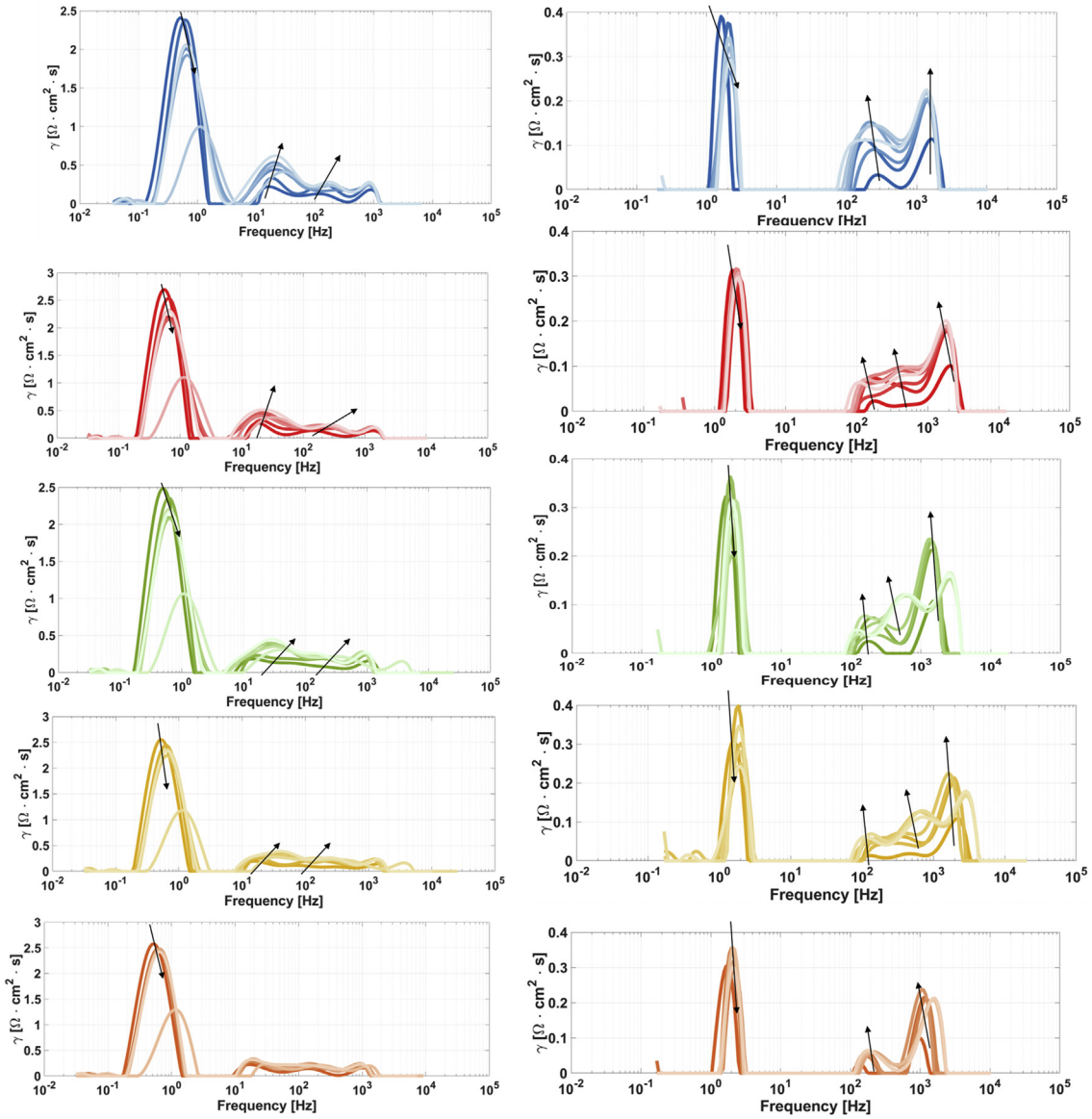

Figure A5 – The distribution of relaxation times for RU1-5 (top to bottom) in SOFC mode (left) and SOEC mode (right) from S1 to S7.

REFERENCES

[1] Boretti A. High-frequency standard deviation of the capacity factor of renewable energy facilities: Part 1—solar photovoltaic. Energy Storage 2020;2:1–8. https://doi.org/10.1002/est2.101.

[2] Miller LM, Keith DW. Addendum: observation-based solar and wind power capacity factors and power densities. Environ Res Lett 2018;13(104008). https://doi.org/10.1088/1748-9326/ab12a2. DOI: 10.1088/1748-9326/aae102). Environmental Research Letters 2019;14.

[3] Irena. IRENA renewable cost database. https://www.irena.org/costs. [Accessed 22 January 2021].

[4] IEA. Coal 2020. Paris: IEA; 2020. 2020, https://www.iea.org/reports/coal-2020. [Accessed 23 January 2021].

[5] World nuclear performance report. 2018.

[6] Trattner A, Klell M, Radner F. Sustainable hydrogen society – vision, findings and development of a hydrogen economy using the example of Austria. Int J Hydrogen Energy 2022;47:2059–79. https://doi.org/10.1016/j.ijhydene.2021.10.166.

[7] Wang L, Zhang Y, Pérez-Fortes M, Aubin P, Lin TE, Yang Y, et al. Reversible solid-oxide cell stack based power-to-x-to-power systems: comparison of thermodynamic performance. Appl Energy 2020;115330:275. https://doi.org/10.1016/j.apenergy.2020.115330.

[8] Reznicek EP, Braun RJ. Reversible solid oxide cell systems for integration with natural gas pipeline and carbon capture infrastructure for grid energy management. Appl Energy 2020;114118:259. https://doi.org/10.1016/j.apenergy.2019.114118.

[9] Mottaghizadeh P, Fardadi M, Jabbari F, Brouwer J. Dynamics and control of a thermally self-sustaining energy storage system using integrated solid oxide cells for an islanded building. Int J Hydrogen Energy 2021;46:24891–908. https://doi.org/10.1016/j.ijhydene.2021.03.136.

[10] Rokni M. Analysis of a polygeneration plant based on solar energy, dual mode solid oxide cells and desalination. Int J

Hydrogen Energy 2019;44:19224–43. https://doi.org/10.1016/j.ijhydene.2018.03.147.
[11] Zhang Z, Zhou J, Zong Z, Chen Q, Zhang P, Wu K. Development and modelling of a novel electricity-hydrogen energy system based on reversible solid oxide cells and power to gas technology. Int J Hydrogen Energy 2019;44:28305–15. https://doi.org/10.1016/j.ijhydene.2019.09.028.
[12] Vialetto G, Noro M, Colbertaldo P, Rokni M. Enhancement of energy generation efficiency in industrial facilities by SOFC – SOEC systems with additional hydrogen production. Int J Hydrogen Energy 2019;44:9608–20. https://doi.org/10.1016/j.ijhydene.2018.08.145.
[13] Luo Y, Li W, Shi Y, Wang Y, Cai N. Reversible H2/H2O electrochemical conversion mechanisms on the patterned nickel electrodes. Int J Hydrogen Energy 2017;42:25130–42. https://doi.org/10.1016/j.ijhydene.2017.08.138.
[14] Wang Y, Li W, Ma L, Li W, Liu X. Degradation of solid oxide electrolysis cells: phenomena, mechanisms, and emerging mitigation strategies—a review. J Mater Sci Technol 2020;55:35–55. https://doi.org/10.1016/j.jmst.2019.07.026.
[15] Khan MZ, Mehran MT, Song RH, Lee SB, Lim TH. Effects of applied current density and thermal cycling on the degradation of a solid oxide fuel cell cathode. Int J Hydrogen Energy 2018;43:12346–57. https://doi.org/10.1016/j.ijhydene.2018.04.175.
[16] Stoeckl B, Subotić V, Preininger M, Schroettner H, Hochenauer C. SOFC operation with carbon oxides: experimental analysis of performance and degradation. Electrochim Acta 2018;275:256–64. https://doi.org/10.1016/j.electacta.2018.04.036.
[17] Sun X, Sudireddy BR, Tong X, Chen M, Brodersen K, Hauch A. Optimization and durability of reversible solid oxide cells. ECS Trans 2019;91:2631–9. https://doi.org/10.1149/09101.2631ecst.
[18] Comminges C, Fu QX, Zahid M, Steiner NY, Bucheli O. Monitoring the degradation of a solid oxide fuel cell stack during 10,000 h via electrochemical impedance spectroscopy. Electrochim Acta 2012;59:367–75. https://doi.org/10.1016/j.electacta.2011.10.080.
[19] Jeanmonod G, Diethelm S, Van herle J. Active near-infrared imaging for spatio-temporal monitoring of a solid oxide cell in operation. ECS Trans 2019;91:437–46. https://doi.org/10.1149/09101.0437ecst.
[20] Peters R, Frank M, Tiedemann W, Hoven I, Deja R, Nguyen VN, et al. Development and testing of a 5kW-class reversible solid oxide cell system. ECS Trans 2019;91:2495–506. https://doi.org/10.1149/09101.2495ecst.
[21] Posdziech O, Schwarze K, Brabandt J. Efficient hydrogen production for industry and electricity storage via high-temperature electrolysis. Int J Hydrogen Energy 2019;44:19089–101. https://doi.org/10.1016/j.ijhydene.2018.05.169.
[22] Mermelstein J, Posdziech O. Development and demonstration of a novel reversible SOFC system for utility and micro grid energy storage. Fuel Cell 2017;17:562–70. https://doi.org/10.1002/fuce.201600185.
[23] Aicart J, Wuillemin Z, Gervasoni B, Reynaud D, Waeber F, Beetschen C, et al. Performance evaluation of a 4-stack solid oxide module in electrolysis mode. International Journal of Hydrogen Energy. https://doi.org/10.1016/j.ijhydene.2021.11.056; 2021.
[24] Frank M, Deja R, Peters R, Blum L, Stolten D. Bypassing renewable variability with a reversible solid oxide cell plant. Appl Energy 2018;217:101–12. https://doi.org/10.1016/j.apenergy.2018.02.115.
[25] Venkataraman V, Pérez-Fortes M, Wang L, Hajimolana YS, Boigues-Muñoz C, Agostini A, et al. Reversible solid oxide systems for energy and chemical applications – review & perspectives. J Energy Storage 2019;24. https://doi.org/10.1016/j.est.2019.100782.
[26] Chi Y, Qiu Y, Lin J, Song Y, Hu Q, Li W, et al. Online identification of a link function degradation model for solid oxide fuel cells under varying-load operation. Int J Hydrogen Energy 2022;47:2622–46. https://doi.org/10.1016/j.ijhydene.2021.10.177.
[27] Kazempoor P, Braun RJ. Model validation and performance analysis of regenerative solid oxide cells for energy storage applications: reversible operation. Int J Hydrogen Energy 2014;39:5955–71. https://doi.org/10.1016/j.ijhydene.2014.01.186.
[28] Zong Z, Zhou J, Zhang Z, Zhao H, Wang J, Ma W, et al. Dynamic analysis of current overshoots in reversible solid oxide cells. Int J Hydrogen Energy 2021;46:34896–911. https://doi.org/10.1016/j.ijhydene.2021.08.048.
[29] Mogensen MB, Chen M, Frandsen HL, Graves C, Hansen JB, Hansen KV, et al. Reversible solid-oxide cells for clean and sustainable energy. Clean Energy 2019;3:175–201. https://doi.org/10.1093/ce/zkz023.
[30] Moçoteguy P, Brisse A. A review and comprehensive analysis of degradation mechanisms of solid oxide electrolysis cells. Int J Hydrogen Energy 2013;38:15887–902. https://doi.org/10.1016/j.ijhydene.2013.09.045.
[31] Zhao Z, Qi H, Tang S, Zhang C, Wang X, Cheng M, et al. A highly active and stable hybrid oxygen electrode for reversible solid oxide cells. Int J Hydrogen Energy 2021;46:36012–22. https://doi.org/10.1016/j.ijhydene.2021.08.150.
[32] Weng F-B, Dlamini MM, Jung G, Lian C-X. Analyses of reversible solid oxide cells porosity effects on temperature reduction. Int J Hydrogen Energy 2020;45:12170–84. https://doi.org/10.1016/j.ijhydene.2020.02.157.
[33] Yang S, Wen Y, Zhang S, Gu S, Wen Z, Ye X. Performance and stability of BaCe0.8−xZr0.2InxO3−δ-based materials and reversible solid oxide cells working at intermediate temperature. Int J Hydrogen Energy 2017;42:28549–58. https://doi.org/10.1016/j.ijhydene.2017.09.159.
[34] Tan Y, Wang A, Jia L, Yan D, Chi B, Pu J, et al. High-performance oxygen electrode for reversible solid oxide cells with power generation and hydrogen production at intermediate temperature. Int J Hydrogen Energy 2017;42:4456–64. https://doi.org/10.1016/j.ijhydene.2016.10.121.
[35] Ahmad MZ, Ahmad SH, Chen RS, Ismail AF, Hazan R, Baharuddin NA. Review on recent advancement in cathode material for lower and intermediate temperature solid oxide fuel cells application. Int J Hydrogen Energy 2022;47:1103–20. https://doi.org/10.1016/j.ijhydene.2021.10.094.
[36] Graves C, Ebbesen SD, Jensen SH, Simonsen SB, Mogensen MB. Eliminating degradation in solid oxide electrochemical cells by reversible operation. Nat Mater 2015;14:239–44. https://doi.org/10.1038/nmat4165.
[37] Yan Y, Fang Q, Blum L, Lehnert W. Performance and degradation of an SOEC stack with different cell components. Electrochim Acta 2017;258:1254–61. https://doi.org/10.1016/j.electacta.2017.11.180.
[38] Lang M, Raab S, Lemcke MS, Bohn C, Pysik M. Long-term behavior of a solid oxide electrolyzer (SOEC) Stack▲. Fuel Cell 2020;20:690–700. https://doi.org/10.1002/fuce.201900245.
[39] Mogensen MB, Chen M, Frandsen HL, Graves C, Hauch A, Hendriksen PV, et al. Ni migration in solid oxide cell electrodes: review and revised hypothesis. Fuel Cell 2021. https://doi.org/10.1002/fuce.202100072.
[40] Königshofer B, Pongratz G, Nusev G, Boškoski P, Höber M, Juričić Đ, et al. Development of test protocols for solid oxide electrolysis cells operated under accelerated degradation

conditions. J Power Sources 2021;229875:497. https://doi.org/10.1016/j.jpowsour.2021.229875.
[41] Wan TH, Saccoccio M, Chen C, Ciucci F. Influence of the discretization methods on the distribution of relaxation times deconvolution: implementing radial basis functions with DRTtools. Electrochim Acta 2015;184:483–99. https://doi.org/10.1016/j.electacta.2015.09.097.
[42] Xia J, Wang C, Wang X, Bi L, Zhang Y. A perspective on DRT applications for the analysis of solid oxide cell electrodes. Electrochim Acta 2020;136328:349. https://doi.org/10.1016/j.electacta.2020.136328.
[43] Caliandro P, Nakajo A, Diethelm S, Van herle J. Model-assisted identification of solid oxide cell elementary processes by electrochemical impedance spectroscopy measurements. J Power Sources 2019;226838:436. https://doi.org/10.1016/j.jpowsour.2019.226838.
[44] Song W, Ma Z, Yang Y, Zhang S, Ou X, Ling Y. Characterization and polarization DRT analysis of direct ethanol solid oxide fuel cells using low fuel partial pressures. Int J Hydrogen Energy 2020;45:14480–90. https://doi.org/10.1016/j.ijhydene.2020.03.146.
[45] Li X, Ahmadi M, Collins L, Kalinin SV. Deconvolving distribution of relaxation times, resistances and inductance from electrochemical impedance spectroscopy via statistical model selection: exploiting structural-sparsity regularization and data-driven parameter tuning. Electrochim Acta 2019;313:570–83. https://doi.org/10.1016/j.electacta.2019.05.010.
[46] Boukamp BA, Rolle A. Use of a distribution function of relaxation times (DFRT) in impedance analysis of SOFC electrodes. Solid State Ionics 2018;314:103–11. https://doi.org/10.1016/j.ssi.2017.11.021.
[47] Jeanmonod G, Diethelm S, Herle JV. The effect of SO2 on the Ni-YSZ electrode of a solid oxide electrolyzer cell operated in co-electrolysis. J Phys Energy 2020;34002:2. https://doi.org/10.1088/2515-7655/ab8b55.
[48] Subotić V, Pofahl S, Lawlor V, Menzler NH, Thaller T, Hochenauer C. Online monitoring tools for SoH diagnostic and prognostic of remaining lifetime of reversible solid oxide cell (rSOC) systems. In: Energy Procedia, vol. 158. Elsevier Ltd; 2019. p. 2329–34. https://doi.org/10.1016/j.egypro.2019.01.271.
[49] Subotić V, Thaller T, Königshofer B, Menzler NH, Bucher E, Egger A, et al. Performance assessment of industrial-sized solid oxide cells operated in a reversible mode: detailed numerical and experimental study. Int J Hydrogen Energy 2020;45:29166–85. https://doi.org/10.1016/j.ijhydene.2020.07.165.
[50] Subotić V, Königshofer B, Juričić Đ Kusnezoff M, Schröttner H, Hochenauer C, et al. Detailed insight into processes of reversible solid oxide cells and stacks using DRT analysis. Energy Convers Manag 2020;113509:226. https://doi.org/10.1016/j.enconman.2020.113509.
[51] Mougin J, Di Iorio S, Chatroux A, Donnier-Marechal T, Palcoux G, Petitjean M, et al. Development of a solid oxide electrolysis stack able to operate at high steam conversion rate and integration into a SOE system. ECS Trans 2017;78:3065–75. https://doi.org/10.1149/07801.3065ecst.
[52] Mougin J, Chatroux A, Couturier K, Petitjean M, Reytier M, Gousseau G, et al. High temperature steam electrolysis stack with enhanced performance and durability. In: Energy Procedia, vol. 29. Elsevier Ltd; 2012. p. 445–54. https://doi.org/10.1016/j.egypro.2012.09.052.
[53] Reytier M, Cren J, Petitjean M, Chatroux A, Gousseau G, Di Iorio S, et al. Development of a cost-efficient and performing high temperature steam electrolysis stack. ECS Trans 2013;57:3151–60. https://doi.org/10.1149/05701.3151ecst.
[54] Reytier M, Di Iorio S, Chatroux A, Petitjean M, Cren J, De Saint Jean M, et al. Stack performances in high temperature steam electrolysis and co-electrolysis. In: International Journal of Hydrogen Energy, vol. 40. Elsevier Ltd; 2015. p. 11370–7. https://doi.org/10.1016/j.ijhydene.2015.04.085.
[55] Di Iorio S, Petitjean M, Petit J, Chatroux A, Gousseau G, Aicart J. SOE stack activities at CEA. In: Proceeding 11th Eur. SOFC Forum Lucerne; 2014.
[56] Leonide A, Apel Y, Ivers-Tiffee E. SOFC modeling and parameter identification by means of impedance spectroscopy. ECS Trans 2009;19:81.
[57] Sumi H, Shimada H, Yamaguchi Y, Yamaguchi T, Fujishiro Y. Degradation evaluation by distribution of relaxation times analysis for microtubular solid oxide fuel cells. Electrochim Acta 2020;135913:339. https://doi.org/10.1016/j.electacta.2020.135913.
[58] Schönleber M, Klotz D, Ivers-Tiffée E. A method for improving the robustness of linear Kramers-Kronig validity tests. Electrochim Acta 2014;131:20–7. https://doi.org/10.1016/j.electacta.2014.01.034.
[59] Iwanschitz B, Sfeir J, Mai A, Schütze M. Degradation of SOFC anodes upon redox cycling: a comparison between Ni/YSZ and Ni/CGO. J Electrochem Soc 2010;157:B269. https://doi.org/10.1149/1.3271101.
[60] Yan D, Zhang C, Liang L, Li K, Jia L, Pu J, et al. Degradation analysis and durability improvement for SOFC 1-cell stack. Appl Energy 2016;175:414–20. https://doi.org/10.1016/j.apenergy.2016.04.094.
[61] Lgj de Haart, Mougin J, Posdziech O, Kiviaho J, Menzler NH. Stack degradation in dependence of operation parameters; the real-SOFC sensitivity analysis. Fuel Cell 2009;9:794–804. https://doi.org/10.1002/fuce.200800146.
[62] Milestones and results - ECo. n.d, Https://WwwEco-Soec-ProjectEu. [Accessed 29 July 2021]. https://www.eco-soec-project.eu/results.
[63] Kim SD, Seo DW, Dorai AK, Woo SK. The effect of gas compositions on the performance and durability of solid oxide electrolysis cells. Int J Hydrogen Energy 2013;38:6569–76. https://doi.org/10.1016/j.ijhydene.2013.03.115.
[64] Klotz D, Weber A, Ivers-Tiffée E. Practical guidelines for reliable electrochemical characterization of solid oxide fuel cells. Electrochim Acta 2017;227:110–26. https://doi.org/10.1016/j.electacta.2016.12.148.
[65] Hjalmarsson P, Sun X, Liu Y-L, Chen M. Durability of high performance Ni–yttria stabilized zirconia supported solid oxide electrolysis cells at high current density. J Power Sources 2014;262:316–22. https://doi.org/10.1016/j.jpowsour.2014.03.133.
[66] Sun X, Hendriksen PV, Mogensen MB, Chen M. Degradation in solid oxide electrolysis cells during long term testing. Fuel Cell 2019;19:740–7. https://doi.org/10.1002/fuce.201900081.
[67] Sampathkumar SN, Sun X, Joris S, Herle JV, Middleton PH, Frandsen HL. Performance analysis of ammonia in solid oxide fuel cells. ECS Trans 2021;185:103. https://doi.org/10.1149/10301.0185ecst.
[68] Leonide André. SOFC modelling and parameter identification by means of impedance spectroscopy. Karlsruhe Institute of Technology; 2010. PhD Thesis.